“© 2025 IEEE. Personal use of this material is permitted. Permission from IEEE must be obtained for all other uses, in any current or future media, including reprinting/republishing this material for advertising or promotional purposes, creating new collective works, for resale or redistribution to servers or lists, or reuse of any copyrighted component of this work in other works.”

Highly Integrated Full-space Coding Metasurface for LP and CP Waves Manipulation Spanning Millimeter-wave and Sub-THz bands

Xiaohui Tan, Rongcao Yang, Shu-Lin Chen *Member, IEEE*, Ka Fai Chan *Member, IEEE*, Bao Jie Chen, Zhao-Qi Cui, Pei-Yuan Qin *Senior Member, IEEE*, Y. Jay Guo, *Fellow, IEEE* and Chi Hou Chan, *Fellow, IEEE*

***Abstract*—Coding metasurfaces (MSs) provide an effective strategy for designing highly integrated devices due to their powerful ability to flexibly manipulate the wavefront of electromagnetic (EM) waves. To date, it remains a great challenge to theoretically construct and experimentally verify highly integrated MSs for manipulating both linear polarization (LP) and circular polarization (CP) waves in full-space at millimeter-wave (mmWave) and sub-terahertz (sub-THz) bands. In this work, a highly-integrated, low-crosstalk, six-channel coding meta-atom is developed using hybrid phase manipulations, which can achieve independent full-space phase controls for three LP channels and three CP channels across three mmWave and sub-THz bands. To validate the concept, we designed and fabricated a compact coding MS, including refracted four-beam splitting for LP wave at 65 GHz; radar cross section (RCS) reduction, anomalous reflection and dual-vortex beam generation for LP and CP waves at 0.12 THz; two-beam splitting for two decoupled CP waves at 0.154 THz. All the theoretical, simulated, and experimental results agree well with each other. The developed highly integrated MS with multiple independent channels presents a promising candidate for future advanced 5G and 6G systems.**

***Index Terms*—coding metasurface, full-space, highly integrated, mmWave and sub-THz**

I. Introduction

METASURFACES (MSs), as typical two-dimensional (2D) planar materials composed of artificial structures with subwavelength dimensions, are distinguished by their negligible electrical thickness, lower insertion loss, and easy fabrication. Moreover, due to their fantastic superiority in manipulating the amplitude, phase, and polarization of electromagnetic (EM) waves [1]–[9], MSs have been promising candidates for increasing high data rates and large capacities in 5G/6G communication systems to demonstrate various practical applications such as polarization converter [10]–[12], efficient chiral mode switching [13], [14], polarization imaging [15], [16], absorber [17]–[19], EM shielding application [20] and so on. In 2014, Cui et al. introduced the coding MS concept and mechanism to manipulate EM waves by comprehensive coding sequences, which not only greatly simplified the design process of MSs, but also suggested a new perspective for connecting the digital and physical worlds [21]. The coding MSs have been rapidly developed, achieving plentiful intriguing functionalities and practical applications such as abnormal refraction/reflection [22], [23], beam steering [24], [25], RCS reduction [26], [27], vortex beam [28], [29] and airy beam generation [30], [31], meta-holograms [32], [33], and many others [34], [35].

Especially, with the rapid development of micro-nano processing technology, EM modulators have gradually tended to miniaturization and high integration, which attracts increasing attention to the research on multifunctional integrated coding MSs [36]–[43]. He et al. constructed a tunable MS, which can respectively manipulate reflected LP and CP wavefronts at different frequencies by varying the conductivity of the VO_2 [36]. Zhang et al. proposed a frequency-multiplexed coding MS, which can independently manipulate surface waves and spatially propagating waves at two frequencies with a shared aperture [38]. Luo et al. constructed an anisotropic polarization-selective passive coding MS with four different functions by manipulating LP and CP waves [40]. Nevertheless, the above-mentioned MSs employing frequency/polarization multiplexing technology can only operate in half-space (transmission or refection space), having limited capacity to regulate EM waves. Very recently, full-space multifunctional coding MSs based on multiplexing technologies [44]–[52] are being explored and developed to satisfy the increasing demands for wireless communication capacity and integrated EM devices. For example, Pan et al. designed a tri-layer multifunctional full-space coding MS for LP wave by independently controlling two co-polarized reflection channels in Ka band and one cross-polarized transmission channel in K-band to achieve three functions [45]. Sun et al. developed a spin- and space-multiplexing MS for full-space manipulation of CP waves to realize four different holographic patterns in four conversion channels in microwave band by incorporating two kinds of metamolecules with opposite asymmetric transmission prop-

This work was supported by National Natural Science Foundation of China (Grant numbers: 62071282), Natural Science Foundation of Shanxi Province (Grant number: 202203021221016) and Innovation and Technology Commission of HKSAR funding support to the State Key Laboratory of Terahertz and Millimeter Waves (City University of Hong Kong) (Project 9448001). *(Corresponding author: Rongcao Yang, Shu-Lin Chen, Chi Hou Chan)*

Xiaohui Tan and Rongcao Yang are with the School of Physics and Electronics Engineering, Shanxi University, Taiyuan 030006, China (e-mail: tanxiaohui0822@163.com; sxdxyrc@sxu.edu.cn).

Shu-Lin Chen, Zhao-Qi Cui, Pei-Yuan Qin and Y. Jay Guo are with the Global Big Data Technologies Centre (GBDTC), University of Technology Sydney (UTS), Ultimo, NSW 2007, Australia (e-mail: shulin.chen@uts.edu.au; Zhaoqi.Cui@student.uts.edu.au; peiyuan.qin@uts.edu.au; Jay.Guo@uts.edu.au).

Ka Fai Chan, Bao Jie Chen and Chi Hou Chan are with State Key Laboratory of Terahertz and Millimeter Waves, City University of Hong Kong, Hong Kong SAR, China (e-mail: kfaichan@cityu.edu.hk; chen.baojie@cityu.edu.hk; eechic@cityu.edu.hk).

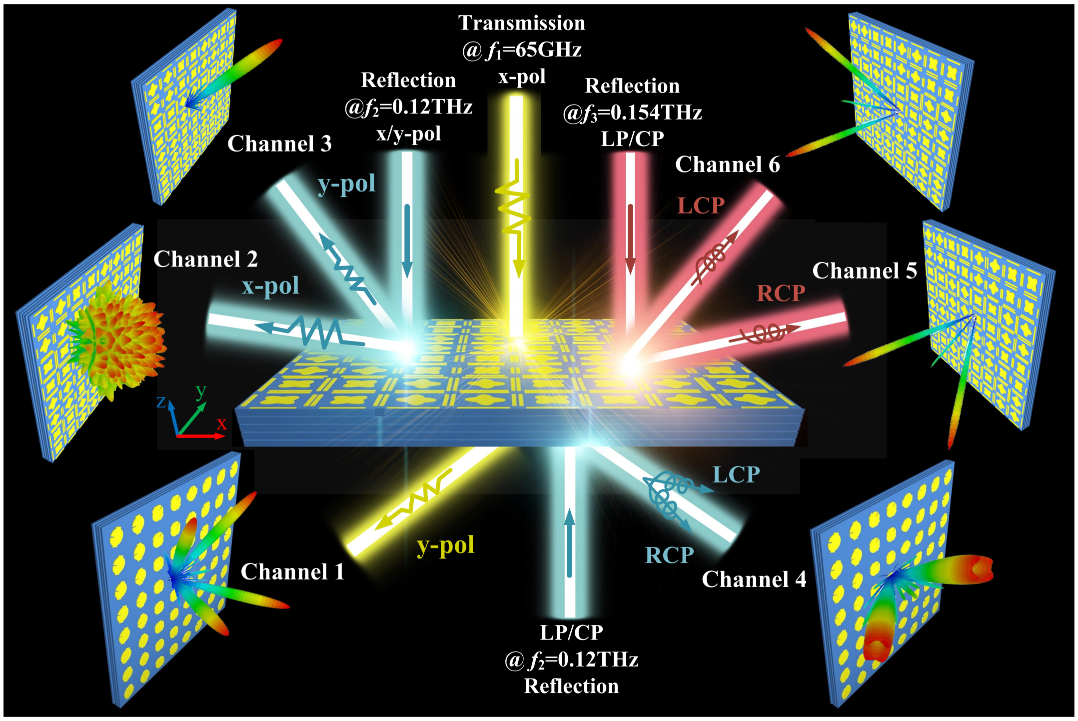

Fig. 1. Schematic diagram of the highly integrated six-channel coding MS.

erties [46]. To further realize full-space manipulation of both LP and CP waves, Fang et al. proposed a trifunctional MS to manipulate the x-polarized wave at 13 GHz and CP waves at 9 GHz in reflection and transmission modes [51].

However, most of multifunctional coding MSs mentioned above focused on the regulation of LP wave or CP wave [37]–[40]. Only a few MSs can regulate both LP wave and CP wave but with limited functions at limited frequency bands [49], [51], due to the coupling among different resonators and the complexity of the coding meta-atomic design. Moreover, these multifunctional MSs are designed and validated at microwave band [40], [42], [44], while mmWave and sub-THz multifunctional MSs are still in simulation stage, especially for full-space multifunctional coding MSs. This may be due to the fact that it is challenging to integrate multiple independent functions in practical manufacturing capability and accuracy since high frequencies will result in physically small MS units, particularly, it is critical when attempting to integrate both mmWave and sub-THz band functions into a single compact MS. In this work, we develop a highly integrated multifunctional coding MS that can realize full-space independent regulation of both LP waves and CP waves via six channels with negligible frequency and polarization crosstalk in mmWave and sub-THz bands

The concept schematic of the developed full-space coding MS is illustrated in Fig. 1. For x-polarized wave propagating along the -z direction at f_1 = 65 GHz (Channel 1), the designed MS can achieve a transmissive four-beam splitting by regulating the geometric phase. For x- and y-polarized waves along the -z direction at f_2 = 0.12 THz (Channels 2 and 3), by modulating the propagation phases, the MS can realize RCS reduction and abnormal reflection, respectively. While for CP wave incidence along +z direction at f_2 = 0.12 THz (Channel 4), dual-vortex beam with topological charge l = +1 and l = -1 can be generated by regulating the geometrical phases. At another sub-THz band f_3 = 0.154 THz, two spin orthogonal CP waves are decoupled by regulating the geometric phase and propagation phase, the reflective right-handed circularly polarized (RCP) wave is split into a dual-beam in the xoz plane (Channel 5), while reflective left-handed circularly polarized (LCP) wave in the yoz plane (Channel 6). The proposed six-channel full-space MS is confirmed through full-wave simulations and prototyping measurements, which is highly promising for future high-speed wireless communication systems.

II. Principle and Meta-atom Design

In order to realize the full-space independent phase control for six channels of LP and CP waves in three mmWave and THz bands, we construct a multilayer meta-atom structure, as shown in Fig. 2. It consists of five copper pattern layers L_1-L_5, interspaced by four identical quartz substrates (ε_r = 3.75, tan δ = 0.007) [53] with a thickness of h = 100 m, as shown in Fig. 2(a). Layer L_1 hosts a centrally located petal-shaped resonator, flanked by two pairs of parallel metal strips on its edges, detailed in Fig. 2(b). Layers L_2 and L_4 consist of mutually perpendicular rectangular metal plates with lengths (p) of 1000 m and widths (k) of 680 m. Layer L_3, shown in Fig. 2(c), incorporates a pair of right-angled resonators positioned face-to-face. And Layer L_5 comprises a split-circle resonator as shown in Fig. 2(d). The dimensions of these metallic structures in Layers L_1- L_5 are detailed in Figs. 2(a)-(d). Their optimized values (in m) are as follows: b = 140, l_1 = 850, l_2 = 600, l_3 = 40, l_4 = 615, w = 60, w_1 = 100, w_2 = 100,

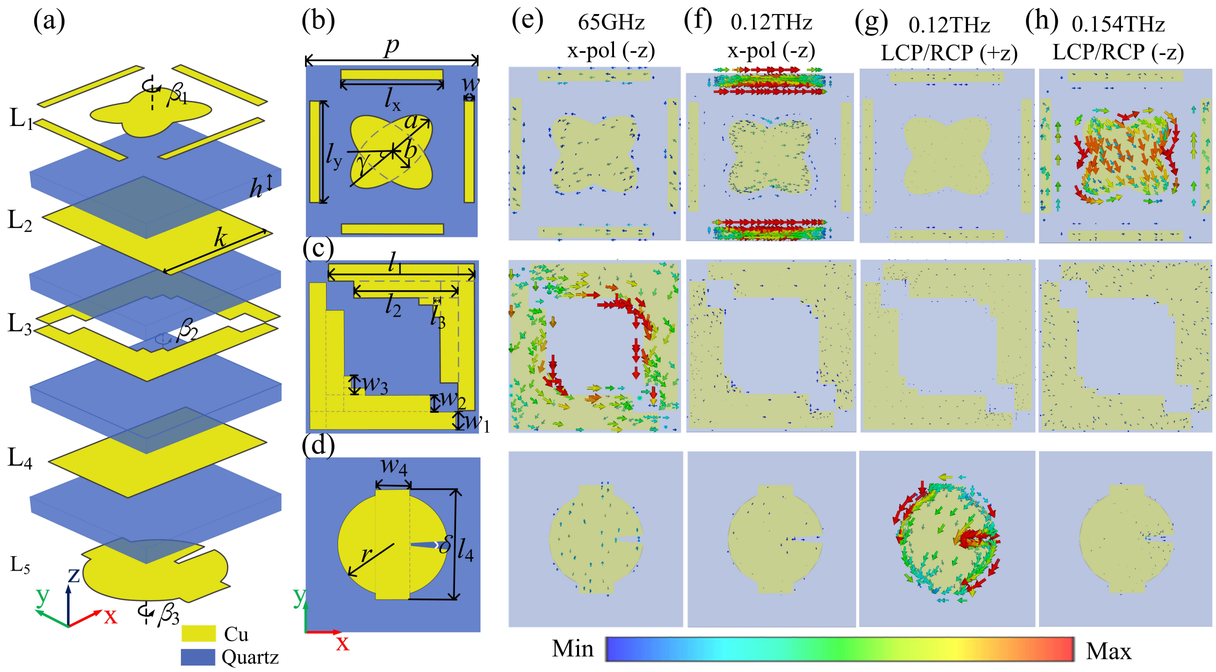

Fig. 2. Geometrical model of meta-atom and corresponding current distributions. (a) Geometrical perspective view. (b-d) Top view of the resonators in Layers L_1, L_3 and L_5. (e-h)Surface current distributions on the resonators under different excitation conditions.

w_3 = 110, w_4 = 200, and r = 270. The angular parameters are set as γ = 40° and δ = 10°. Additionally, the designed meta-atom can be divided into three parts: the reflective sub-cell in the -z direction (Layers L_1 and L_2), the bidirectional transmissive sub-cell (Layers L_2, L_3 and L_4), and the reflective sub-cell in the +z direction (Layers L_4 and L_5). For the two reflective sub-cells, Layers L_2 and L_4 are used as bidirectional reflector plates to reflect EM waves propagating along the -z and +z direction, while for the bidirectional transmissive sub-cell, Layers L_2 and L_4 can be formed a Fabry-Perot cavity along with Layer L_3 to generate a transmissive polarization conversions. Layer L_1 with two pairs of parallel metal strips and a petal-shaped resonator is used to regulate the reflected orthogonal LP wave at 0.12 THz and orthogonal CP wave at 0.154 THz. Layer L_3 with right-angled resonators is used to regulate the transmitted orthogonal LP wave at 65 GHz. And Layer L_5 with split-circle resonator is used to regulate the reflected orthogonal CP wave at 0.12 THz.

The CST microwave studio is used for full-wave simulations to characterize the reflection and transmission characteristics of the meta-atom by setting periodic boundaries in x and y directions, open boundary in z direction and applying floquet-port excitation. We firstly simulate the current distributions with the following parameter values: l_x = l_y = 652 m, a = 300 m, and β_1 = β_3 = 0°, β_2 = 45° to investigate the response mechanism of each resonator layer. As shown in Fig. 2(e), when the incidence is the x-polarized wave along -z direction at f_1 = 65 GHz, the strong currents are excited on the right-angled resonator on Layer L_3. With the same incidence, the currents are concentrated on the pair of metal strips parallel to the x direction on Layer L_1 at f_2 = 0.12 THz as depicted in Fig. 2(f). Obviously, for the incident y-polarized wave, the currents will be distributed on the strips parallel to the y direction on Layer L_1. When the LCP/RCP wave at 0.12 THz is incident along +z direction, the currents are concentrated on the split-circle resonator on Layer L_5, as shown in Fig. 2(g). While the LCP/RCP wave is incident along -z direction at f_3 = 0.154 THz, the induced currents are distributed on the petal-shaped resonator on Layer L_1, as plotted in Fig. 2(h). This means that the EM responses of the designed meta-atom demonstrate a precise correspondence with the intended resonators across the metal layers, tailored for incident waves of different frequencies, polarizations, and directions. It is noted that the characteristics of the meta-atom can be independently regulated by fine-tuning the parameters l_x, l_y, a, β_1, β_2 and β_3.

The working principle of the meta-atom can be analyzed by using the Jones matrix J in Cartesian coordinates, which facilitates the simultaneous investigation of both the propagation phase and geometrical phase modulation of the resonators. The Jones matrix can be expressed as [54]:

$$J = M^{-1}(\beta)\begin{pmatrix} |R_{xx}|\,e^{i\varphi_{xx}} & |R_{xy}|\,e^{i\varphi_{xy}} \\ |R_{yx}|\,e^{i\varphi_{yx}} & |R_{yy}|\,e^{i\varphi_{yy}} \end{pmatrix} M(\beta) \qquad (1)$$

where $M(\beta) = \begin{pmatrix} \cos\beta & -\sin\beta \\ \sin\beta & \cos\beta \end{pmatrix}$ stands for the rotation matrix and β is the rotation angle of the resonator. $|R_{xx}|$ and $|R_{yy}|$ represent the reflection amplitudes of co-polarized waves, $|R_{yx}|$ and $|R_{xy}|$ represent the reflection amplitudes of cross-polarized waves for x- and y-polarized waves, respectively. As previously mentioned, the strip pair on Layer L_1 can respond to the incident waves propagating along -z direction at f_2 = 0.12 THz. Figs. 3(a)-(d) show the reflection amplitudes and phases by varying l_x within 570-750 m and l_y within

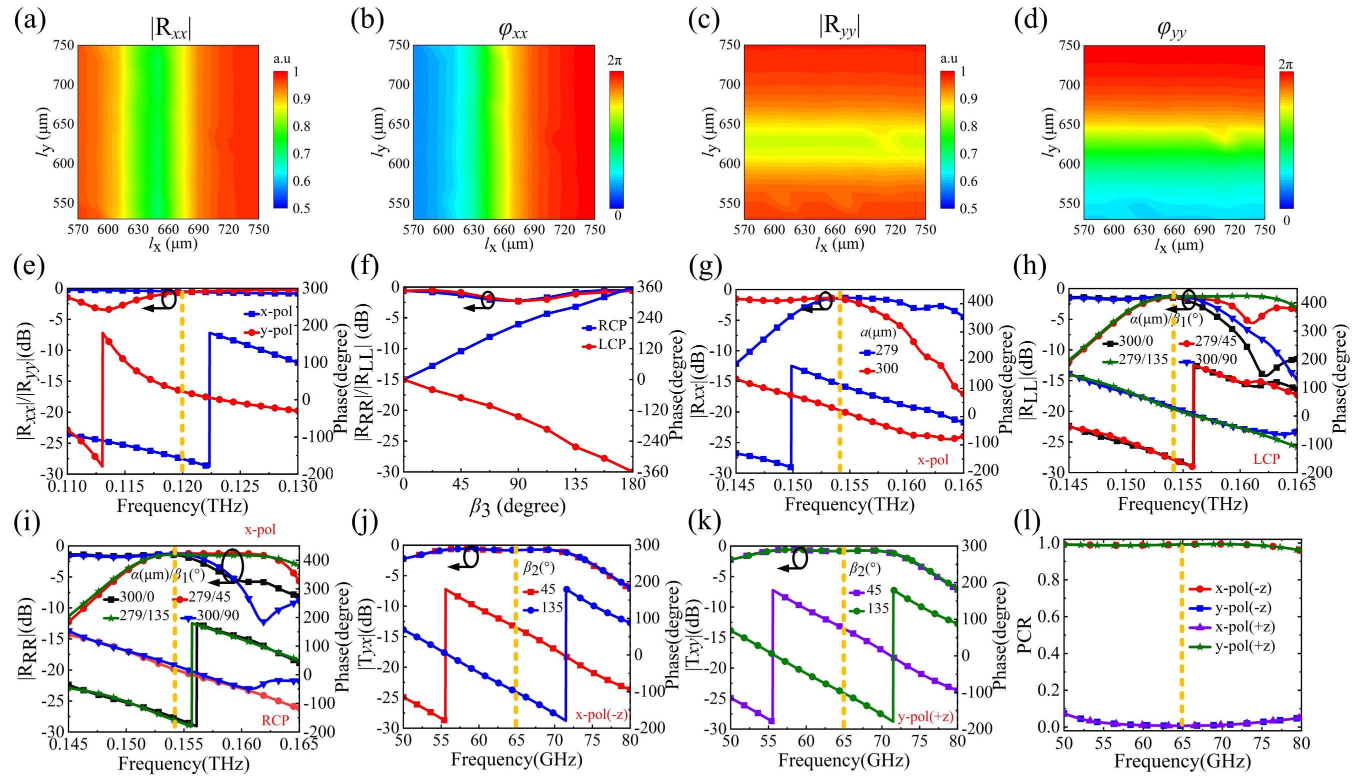

Fig. 3. Transmission and reflection properties of the coding meta-atoms. (a)-(d) Reflection properties for the x- and y-polarized waves along -z direction at f_2 when changing l_x and l_y. (e)Reflection properties for the x- and y-polarized waves along +z direction at f_2 and phase responses for (f) LCP and RCP waves when changing β_3. (g) Reflection properties for the x-polarized wave along -z direction at f_3 when varying a and reflection properties of 1-bit spin-decoupled coding meta-atoms for (h) LCP and (i) RCP waves when varying a and β_1. Transmission properties for (j) the x-polarized wave along -z direction and (k) the y-polarized wave along +z direction at f_1 when changing β_2, and (l) PCR for x- and y-polarized waves.

550-750 m for the incident x- and y-polarized waves at 0.12 THz, respectively. It can be clearly seen that the reflection amplitudes are all over 0.8 while the reflection propagation phases cover a full 360° range at f_2 = 0.12 THz. To implement 2-bit encoding, we select coding meta-atoms with l_x =575 m, 635 m, 652 m, 688 m and l_y = 572 m, 618 m, 652 m, 880 m for propagation phase modulation to regulating the x-polarized and y-polarized waves, respectively. Moreover, it is clearly seen that there is a good isolation between the two modes, which guarantees independent wavefront operation to suppress polarization crosstalk. Therefore, according to Equation. (1), the Jones matrix J_1 can be written as a function of l_x and l_y:

$$J_1(l_\mathrm{x}, l_\mathrm{y}) = \begin{pmatrix} e^{i\varphi_{\mathrm{xx}}^{l_\mathrm{x}}} & 0 \\ 0 & e^{i\varphi_{\mathrm{yy}}^{l_\mathrm{y}}} \end{pmatrix} \quad (2)$$

When the EM wave is incident along +z direction, responding on the sub-cell (Layers L_4 and L_5), there exhibits high co-polarized reflection amplitudes and possesses 180° phase difference for the x- and y-polarized waves at f_2 = 0.12 THz, as shown in Fig. 3(e), indicating that the reflective sub-cell (Layers L_4 and L_5) can form a perfect half-wave plate. The Jones matrix J_2 for half-wave plate with the rotation angle β_3 can be expressed as:

$$J_2(\beta_3) = \begin{pmatrix} \cos 2\beta_3 & \sin 2\beta_3 \\ \sin 2\beta_3 & -\cos 2\beta_3 \end{pmatrix} \quad (3)$$

For the incident CP wave $E_{\mathrm{CP}}^{in} = \frac{1}{\sqrt{2}}\binom{1}{\pm i}$, the output reflected component E_{CP}^{out} can be written as $E_{\mathrm{CP}}^{out} = \frac{1}{\sqrt{2}} e^{\pm i2\beta_3} \begin{pmatrix} 1 \\ \mp i \end{pmatrix}$, where "+" and "-" represent the RCP and LCP waves, respectively. Both the output RCP and LCP waves have an additional $2\beta_3$ geometric phase change by varying the parameter β_3. Fig. 3(f) shows the phase and amplitude for the case of 3-bit encoding. Eight coding states are obtained by adjusting β_3 in 22.5° increments and the geometric phase differences between the neighboring states are about +45° and -45° for the incident RCP and LCP waves . Furthermore, when the propagation phase and geometric phase are regulated simultaneously by changing the parameter a and the rotation angle β_1 of the petal-shaped resonator on Layer L_1, two spin decoupling channels for the RCP and LCP waves at f_3 = 0.154 THz can be achieved. The corresponding Jones matrix J_3 can be written as:

$$J_3(a, \beta_1) = \begin{pmatrix} \cos 2\beta_1 e^{i\varphi_{xx}^a} & \sin 2\beta_1 e^{i\varphi_{xx}^a} \\ \sin 2\beta_1 e^{i\varphi_{xx}^a} & -\cos 2\beta_1 e^{i\varphi_{xx}^a} \end{pmatrix} \quad (4)$$

Under the CP wave incidence, the output waves can be represented as $E_{\mathrm{CP}}^{\mathrm{out}} = \frac{1}{\sqrt{2}} e^{i(\varphi_{\mathrm{xx}}^a \pm 2\beta_1)} \begin{pmatrix} 1 \\ \mp i \end{pmatrix}$. From the phases $\varphi_{\mathrm{RR}} = \varphi_{\mathrm{xx}}^a + 2\beta_1$ and $\varphi_{\mathrm{LL}} = \varphi_{\mathrm{xx}}^a - 2\beta_1$, the required propagation phase φ_{xx}^a and the rotation angle β_1 can be

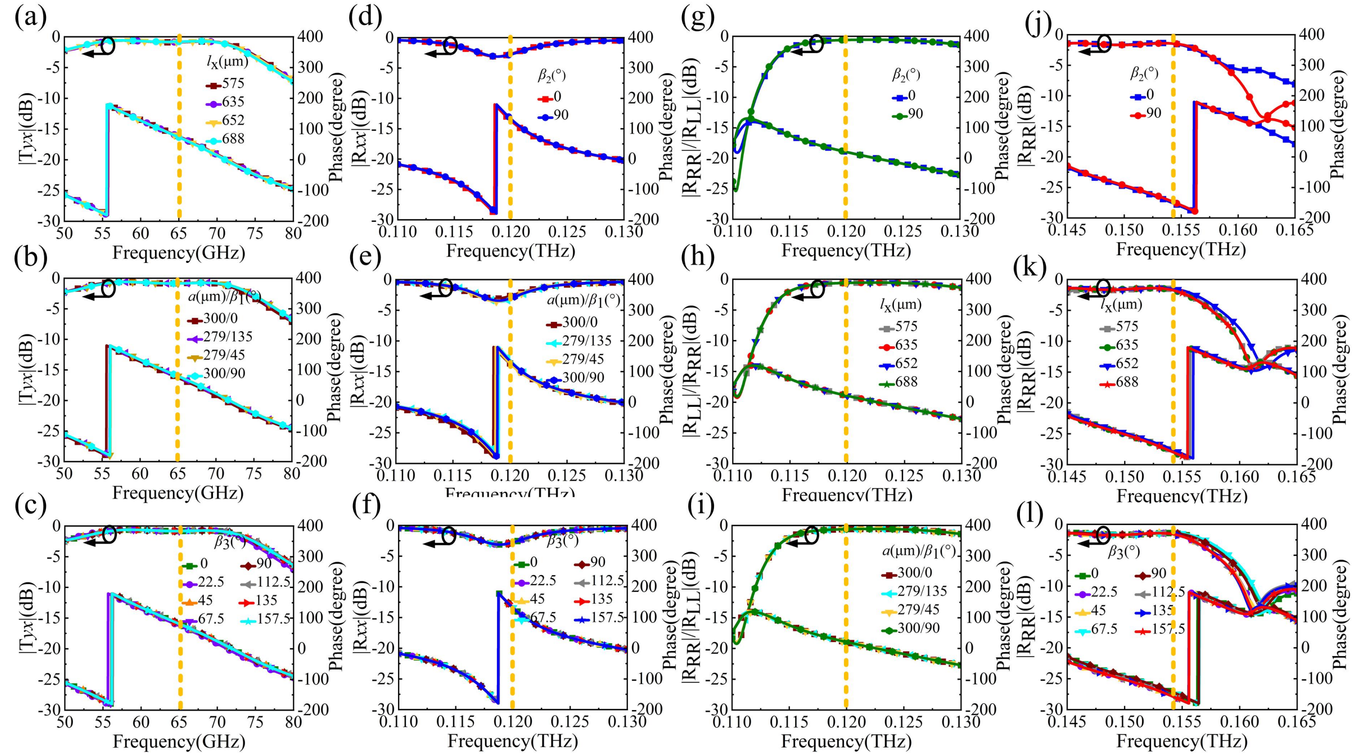

Fig. 4. Crosstalk on the transmission and reflection properties of coding meta-atoms. Transmission properties for the x-polarized wave at f_1 when changing (a) l_x, (b) a, β_1, and (c) β_3. Reflection properties for the x-polarized wave at f_2 when changing (d) β_2, (e) a, β_1, and (f) β_3. Reflection properties for the RCP/LCP wave at f_2 when changing (g) β_2, (h) l_x, and (i) a, β_1. Reflection properties for the RCP/LCP wave at f_3 when changing (g) β_2, (h) l_x, and (i) β_3.

calculated as:

$$\varphi^a_{\rm xx} = (\varphi^a_{\rm LL} + \varphi^a_{\rm RR})/2 \tag{5}$$

$$\varphi^a_{\rm yy} = (\varphi^a_{\rm LL} + \varphi^a_{\rm RR})/2 - \pi \tag{6}$$

$$\beta_1 = (\varphi_{\rm RR} - \varphi_{\rm LL})/4 \tag{7}$$

Thus, one can obtain the phase parameters of the 1-bit spin-decoupled coding meta-atoms, as shown Tab. I.

TABLE I
PHASE PARAMETERS OF 1-BIT SPIN-DECOUPLED META-ATOMS

$\varphi_{\rm RR}/\varphi_{\rm LL}$	$\varphi_{\rm LL} = 0°(0)$	$\varphi_{\rm LL} = 180°(1)$
$\varphi_{\rm RR} = 0°(0)$	$\varphi^a_{xx} = 0°$, $\beta_1 = 0°(0/0)$	$\varphi^a_{xx} = 90°$, $\beta_1 = 135°(0/1)$
$\varphi_{\rm RR} = 180°(1)$	$\varphi^a_{xx} = 90°$, $\beta_1 = 45°$ (1/0)	$\varphi^a_{xx} = 0°$, $\beta_1 = 90°$ (1/1)

Through analyzing Tab. I, it is easy to know that the 1-bit coding meta-atoms for realizing spin decoupling can be formed by two half-wave plates with a phase difference of 90°. As shown in Fig. 3(g), when the parameter a is set as 279 m and 300 m with β_1 fixed at 45°, high amplitudes $|R_{yx}|$ and 90° phase difference are observed at f_3 = 0.154 THz for the x-polarized wave incidence along the -z direction, indicating that the two states satisfy the spin decoupling condition. Fig. 3(h) depicts the reflective amplitudes and phases of the four meta-atoms shown Tab. I under the LCP wave incidence. It is observed from Fig. 3(h), at 0.154 THz, the phase difference between the two states encoding 0/0 (a=300 m, β_1=0°) and 0/1 (a=279 m, β_1=135°) is about 180°, while for those encoding 0/0 (a=300 m, β_1=0°) and 1/0 (a=279 m, β_1=45°), the phase difference is 0°. Conversely, under the RCP wave incidence, the situation is reversed, as evidenced in Fig. 3(i). These results confirm that the LCP and RCP waves can be spin decoupled, aligning well with theoretical predictions.

The designed meta-atom can also operator in bidirectional transmissive mode for the LP wave at 65 GHz. Specifically, the meta-atom can realize LP conversion for the x-polarized wave propagating along -z direction and y-polarized wave propagating along +z direction, respectively. Fig. 3(j) shows that the phase and amplitude of transmission coefficient T_{yx} for the x-polarized incident wave along -z direction from 50 to 80 GHz when the rotation angle β_2 of the right-angled resonators on Layer L_3 is set as 45° and 135°. It is observed that high cross-polarization transmission amplitude and 180° phase shift are achieved for the two different rotation angle β_2. This aligns perfectly with the criteria for 1-bit transmission encoding. Correspondingly, for the y-polarized incident wave propagating along +z direction, high transmission amplitudes and 180° phase difference can be realized, as shown in Fig. 3(k). The conversion efficiency is quantifiable by the polarization conversion rate (PCR), defined as PCR $= \left|t^2_{ji}\right| / \left(\left|t^2_{ji}\right| + \left|t^2_{ii}\right|\right)$, where t_{ji} and t_{ii} are the cross-polarization and co-polarization transmission coefficients, respectively [45]. As shown in Fig. 3(l), when the LP wave is incident along $-z(+z)$ direction, the PCR is approximately equal to 1 for $x(y)$-polarized wave and 0 for $y(x)$-polarized wave ranging from 50 to 80 GHz. This means the meta-atom possesses good ability of bidirectional polarization conversion in the mmWave band in transmission mode.

As demonstrated above, phase manipulation of the six channels can be realized in three different frequency bands by regulating the parameters l_x, l_y, a, β_1, β_2 and β_3 based on phase modulation theories. Notably, the study of crosstalk is greatly significant for the design of coding meta-atoms, as it directly affects or even destroy the performance of multi-functional integrated coding MS operating independently in different Channels. We study the crosstalk on the transmissive and reflective characteristics of meta-atom at the three bands of 65 GHz, 0.12 THz and 0.154 THz, as shown in Fig. 4. It is clear to see that for the x-polarized wave along -z direction, the transmissive amplitude and phase are hardly affected by the variations of l_x, a, β_1 and β_3 at 65 GHz, as shown in Figs. 4(a)-(c), and there is only negligible reflective amplitude and phase variations for different a, β_1, β_2 and β_3 at 0.12 THz, as shown in Figs. 4(d)-(f). The crosstalk on the reflective characteristics of meta-atom for the CP waves incident along +z direction at 0.12 THz is depicted in Figs. 4(g)-(i). The variations of the parameters a, β_1, β_2 and l_x have almost no influence on the reflection amplitude and phase. Also, as displayed in Figs. 4(j)-(l), regulating l_x, β_2 and β_3 has also no effect on the reflective characteristics for the CP waves incident along -z direction at 0.154 THz. Therefore, based on the hybrid manipulation principles of propagation phase and geometric phase, the designed coding meta-atom not only satisfies the requirements of high amplitude and superior 360° phase shift, but also has good isolation properties among different modes, which provides a good foundation for independent regulation of multi-channel EM waves.

III. Integrated Multifunctional Coding MS

To verify the performance of the designed coding meta-atoms, as a proof of concept, we construct a full-space six-channel multiplexing coding MS composed of 32×32 meta-atoms to endow six-fold functions with a shared aperture as follows: four-beam splitting for the x-polarized wave at f_1 = 65 GHz (Channel 1), RCS reduction, abnormal reflection and dual-vortex beam generation for the x-polarized, y-polarized and CP waves at f_2 = 0.12 THz (Channels 2, 3 and 4), dual-beam splitting in the xoz plane and yoz plane for the decoupled RCP and LCP waves at f_3 = 0.154 THz (Channels 5 and 6). The corresponding phase distributions Φ_1-Φ_6 for the six channels (Channels 1-6) are shown in Figs. 5(a)-(e), and the three-dimensional (3D) layout of the integrated coding MS with a total size 32 mm ×32 mm and a thickness of 0.40 mm is shown in Fig. 5(f), and the top view of resonators Layers L_1, L_3 and L_5 are shown in Figs. 5(g)-(i), respectively. The far-field scattering properties of the designed coding metasurface are simulated by CST microwave studio with open boundary conditions in all directions and plane wave excitation.

For Channel 1, the 1-bit checkerboard coding sequence shown in Fig. 5(a), where each lattice with different parameter β_2 composed of 4×4 meta-atoms, is designed to achieve four symmetrical y-polarized beams splitting for the incident x-polarized waves. The 3D far-field pattern is depicted in Fig. 6(a). The elevation angle θ and azimuth angle φ can be theoretically calculated by the formula $\theta = \sin^{-1}\left(\lambda\sqrt{1/\Gamma_x^2 + 1/\Gamma_y^2}\right)$ and $\varphi = \pm\tan^{-1}(\Gamma_x/\Gamma_y)$ [55], where λ is the operating wavelength, Γ_x and Γ_y are the periodic lengths of the coding sequence along the x and y directions, respectively. The calculated elevation angle θ is ±54.7° and azimuth angle φ are ±45° and ±135° at f_1 = 65 GHz. The simulated 2D far-field patterns at the cross section of φ = 45 ° and 135° are presented in Figs. 6(b) and (c), respectively, where the maximum intensity is at θ = ±54.7°, which are well consistent with the theoretical calculations. As shown in Figs. 5(b) and (c), the 2-bit rotated random coding sequence with different parameters l_x and gradient coding sequence with different parameters l_y are designed to realize RCS reduction and abnormal reflection for the x- and y-polarized waves incidence at f_2 = 0.12 THz in Channels 2 and 3, respectively. To illustrate the performance of RCS reduction, Figs. 6(d) and (e) respectively shown the simulated 3D far-field patterns of the coding MS and the same-sized metallic plate. In contrast to the vertical reflection by the metal plate, the incident x-polarized wave is reflected in multiple random directions by the coding MS. This comparison is further highlighted for the coding MS and the metal plate, as shown in Fig. 6(f), where a -20.3 dB RCS reduction is achieved by the coding MS. While for the y-polarized wave incident to the coding MS, the reflected co-polarized wave is abnormally deflected into the specific pointing beam in yoz plane, as depicted in Fig. 6(g). The corresponding electric field

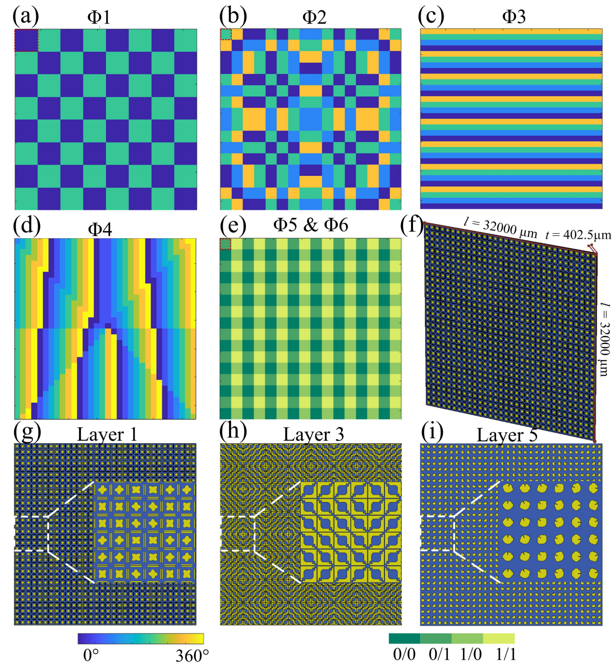

Fig. 5. Diagram of phase distributions and layouts of the developed integrated MS. (a-e) phase distributions Φ_1-Φ_6 of Channels 1-6, (f) 3D layout and (g-i) Top view of Layers L_1, L_3 and L_5.

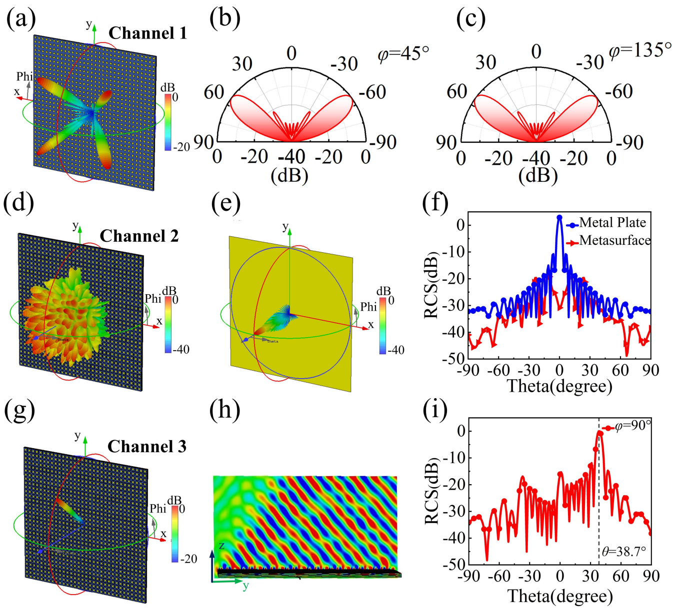

Fig. 6. Simulated far-field radiation characteristics of Channel 1 at f_1 = 65 GHz, and Channels 2 and 3 at f_2 = 0.12 THz. (a) 3D far-field pattern, and 2D far-field pattern at cross section (b) φ = 45° and (c) φ = 135° for x-polarized waves incidence along -z direction at f_1. (d, e) 3D far-field patterns and (f) 2D far-field patterns of the coding MS and metal plate for the x-polarized wave incidence along -z direction at f_2. (g) 3D far-field pattern, (h) electric field distribution, and (i) 2D far-field pattern for the y-polarized waves incidence along -z direction at f_2.

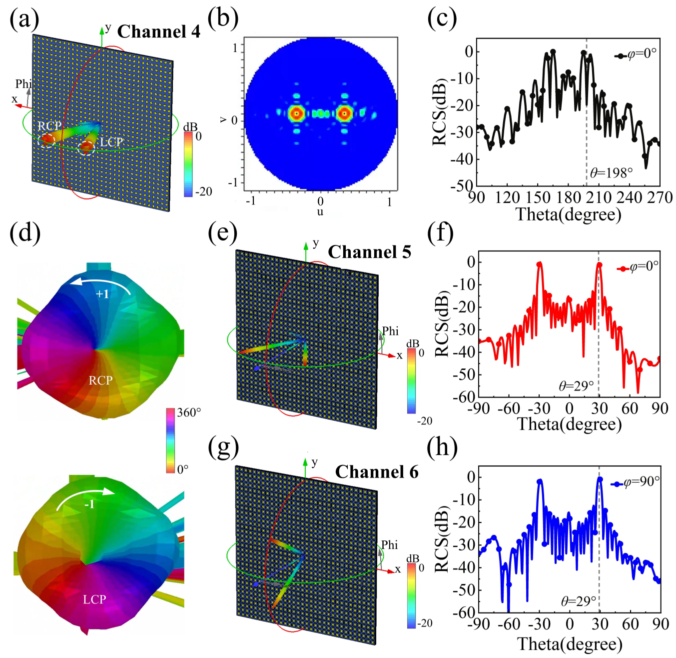

Fig. 7. Simulated far-field radiation characteristics of Channel 4 at f_2 = 0.12 THz, and Channels 5 and 6 at f_3 = 0.154 THz. (a) 3D far-field pattern, (b) 2D intensity distribution, (c) 2D far-field pattern, and (d) phase distributions of the total far-field scattering characteristics for the x-polarized waves incidence along the +z direction at f_2. (e, g) 3D far-field pattern and (f, h) 2D far-field pattern for the RCP and LCP waves incidence along -z direction at f_3.

distribution and 2D far-field pattern of the abnormal reflected beam at the cross section of φ=90° are plotted in Figs. 6(h) and (i), where the simulated reflected y-polarized wave is deflected at an angle of 38.7°. It is consistent with the theoretical value θ = 38.7° calculated by the formula $\theta = \sin^{-1}(\lambda/\Gamma)$ of generalized Snell's laws [22].

Furthermore, the 3-bit mixed coding sequence with different rotation angles β_3 in Fig. 5(d), which is formed by the gradient coding sequence "01234567…" and the rotated vortex coding sequence with orbital angular momentum models of l = +1 and l = -1, is designed to facilitate the double vortex beams generation in Channel 4 for the CP wave along +z direction at f_2 = 0.12 THz. As shown in Figs. 7(a)-(c), the incident RCP and LCP waves are split into two symmetric hollow vortex beams at the deflection angles of 18.2° in the xoz plane, which agrees with the theoretically prediction. Apparently, the left and right vortex beams are generated by the RCP and LCP waves, respectively. Fig. 7(d) depicts that the spiral phase of the two vortex beams varies from 0 to 360°, carrying orbital angular momentum modes l = +1 and l = -1. Finally, for Channels 5 and 6, the 1-bit spin decoupled square coding array in Fig. 5(e) with different parameter a and β_1 is constructed to realize dual-beam splitting in two orthogonal planes for the decoupled RCP and LCP waves at f_3 = 0.154 THz. It can be seen from Figs. 7(e) and (g) that two symmetrical beams are generated in the xoz and yoz planes for the RCP and LCP waves at f_3 = 0.154 THz, respectively. The simulated elevation angles θ of the LCP wave at the cross section of φ = 0° and the RCP wave at the cross section of φ = 90° are both 29°, which are shown in Figs. 7(f) and(h). This is well in agreement with the theoretically calculated deflection angle θ = ±29.1° at f_3 = 0.154 THz according to the generalized Snell's laws, implying that the LCP and RCP waves can be decoupled by the designed MS, and have a good isolation performance.

IV. Experiment Verification

Experimental verification is crucial for validating the performance of a designed MS. However, to our knowledge, most current MS designs in the THz bands remain at the simulation stage. Experimentally validating a design in the THz band presents significant challenges, not only due to the inherent difficulties in THz manufacturing but also because of the stringent tolerance requirements, as small inaccuracies can lead to substantial deterioration in experimental results. This, in turn, raises higher requirements for THz designs. Our design, which integrates both sub-THz and mmWave functions into a single multilayer structure, poses additional challenges for fabrication while maintaining high accuracy. Additionally, measuring sub-THz designs requires a high level of accuracy, particularly in alignment. Our integrated design necessitates more sophisticated measurement platforms that can accommodate both mmWave and sub-THz bands.

To address these challenges in experimental verification of our design, we have employed precise fabrication techniques and comprehensive facility setups to ensure accurate fabrication and measurement of the developed MS. The fabricated prototype is shown in Fig. 8(a) with the microscopic images depicted in Figs. 8(b) and (c). The fabrication processes are carried out using the micromachining method available at the City University of Hong Kong (CityU) [56]. The multilayer structure is formed by stacking the substrate and copper layers sequentially from the bottom to the top, resembling a sandwich structure. The alignment process was accomplished by using the MA/BA Gen4-Serie Mask- und Bond-Aligner from the SUSS MicroTec Group. After the alignment, the substrate was bonded using UV curable glue. This way the multiple metal layers can be accurately aligned. The accuracy for the copper pattern on each layer is 0.5 μm and the error is within 0.5%. Moreover, benefiting from the transparency of the quartz substrates, all five metal layers are precisely aligned, minimizing potential measurement performance deterioration. In addition, we implemented two separate measurement setups to ensure the accurate measurement of the multiple independent functions across mmWave and sub-THz bands. This includes a robotic six-axis mmWave system depicted in Fig. 8(d) and a sub-THz experimental measurement platform shown in Fig. 8(e), which are all located at the State Key Laboratory of Terahertz and Millimeter Waves (SKLTMW), CityU.

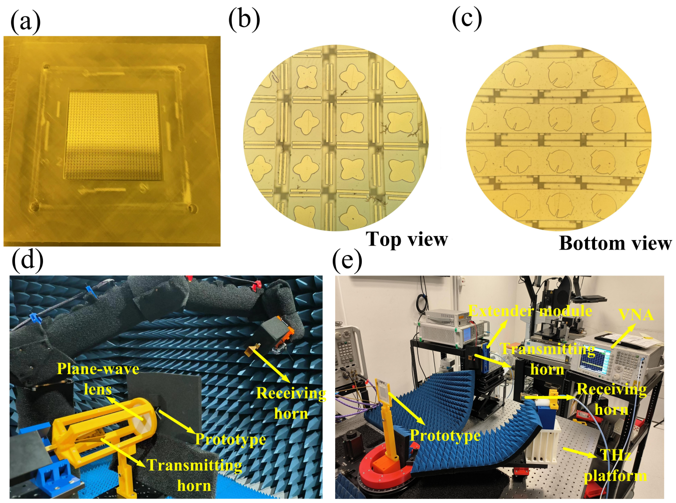

Fig. 8. Photographs of fabricated MS prototype and experimental setups. (a) MS prototype, (b) top view and (c) bottom view. Experimental setups for meas-urements of (d) transmission mode and (e) reflection mode.

Specifically, the setup in Fig. 8(d) is utilized for measuring the transmission mode in the mmWave band (Channel 1). The transmitting and receiving horns are placed on the front and back sides of the MS prototype, respectively. And absorbing materials are placed around those to mitigate the spillover effect of the incident waves on the receiving side. Both the transmitting and receiving horns are connected to OML extenders to cover the 50-75 GHz mmWave band. In addition, a plane-wave lens is used to generate the plane-wave incidence on the MS, and the receiving antenna is positioned in the farfield region of the MS to ensure measurement accuracy. The horns are linearly polarized and they can be freely rotated by the robotic arm to control the transmitting/receiving polarization. In Channel 1, the transmitting horn is rotated to be x polarization and the receiving horn is rotated to be y polarization. To achieve the desired transmitting pattern, the receiving horn is scanned with respect to the center of the MS during the measurement. For the reflection modes in the sub-THz bands, the THz measurement platform setup shown in Fig. 8(e) is employed with both transmitting and receiving horns placed on the same side. Two OML extender modules are used to measure the two bands at 0.12 THz (Channel 2-4) and 0.154 THz (Channels 5 and 6), respectively. Similarly, the transmitting and receiving horns for Channels 2-4 can be also freely rotated by the robotic arm to vary the LP states, and the receiving horn is scanned to measure far-field scattering characteristics of the reflected LP responses. While for the CP responses of Channels 5 and 6, the LP responses are measured firstly by the same way, and then the RCP and LCP responses are calculated with $E_{RCP} = \frac{\sqrt{2}}{2}\left(E_x + iE_y\right)$ and $E_{LCP} = \frac{\sqrt{2}}{2}\left(E_x - iE_y\right)$ [46]. It is worth noting that the far-field scattering characteristics with elevation angles of -15°-15° are not measured because the reflecting and receiving horns are located on the same side of the MS sample in the reflection modes.

Fig. 9 presents the 2D farfield patterns of the simulated and experimental results for Channels 1-6. For the x-polarized waves incidence at $f_1 = 65$ GHz, both the simulated and measured transmitted beams are strictly pointed at 54.7°, as shown in Fig. 9(a). The experimental results are in good agreement with the simulated ones. For the x- and y-polarized waves at $f_2 = 0.12$ THz, the simulated and measured results for Channels 2 and 3 are shown in Figs. 9(b) and (c), respectively. The x-polarized reflection wave is randomly scattered in multiple directions, while the y-polarized reflection wave is deflected at about 38.7°, where the experimental results are well consistent with the simulated and theoretical ones. When the x-polarized wave at $f_2 = 0.12$ THz is incident towards the designed MS from the opposite direction for Channel 4, double vortex beams are generated with an elevation angle θ of about ±18.2°, as shown in Fig. 9(d), which is in a good agreement with the simulated and theoretical ones. Finally, as displayed in Figs. 9(e) and (f) for Channels 5 and 6, symmetry beam splitting occurs in the xoz plane for the decoupled RCP wave incidence at $f_3 = 0.154$ THz, while for the decoupled LCP wave incidence, symmetry beam splitting occurs in the yoz plane, where the deflection angles produced by both the RCP and LCP waves are 29°. It is noted that the far-field scattering characteristics of elevation angles of -15°-15° cannot be measured in all reflection modes as the transmitting and receiving horns are positioned on the same side of the prototype. Additional discrepancies between simulated and experimental results at the measured range can be attributed primarily to fabrication inaccuracies and measurement tolerances, which are particularly challenging in the sub-THz bands. All experimental results of the fabricated MS for transmitted and reflected EM waves indicate that the developed coding MS can efficiently realize six-channel independent manipulation of EM waves in three mmWave and THz bands.

V. Conclusion

In conclusion, we have developed and fabricated a high integrated six-channel full-space passive coding MS with a single shared aperture, which can independently manipulate the transmitted and reflected in three mmWave and sub-THz

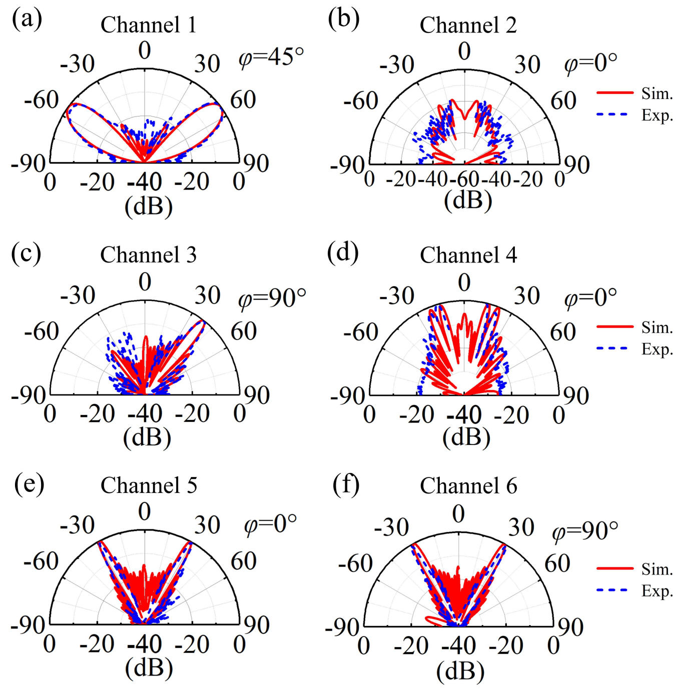

Fig. 9. Measured and simulated 2D far-field patterns of the coding MS for Channel 1-6. (a) Channel 1: four-beam splitting in transmission mode, for reflection mode (b) Channel 2: RCS reduction, (c) Channel 3: abnormal reflection, (d) Channel 4: double vortex beams generation, beam splitting (e) Channel 5: in the xoz plane and (f) Channel 6: in the yoz plane.

bands. The designed meta-atom has excellent properties of efficient polarization isolation and frequency isolation. By regulating the propagation phase and geometrical phase, the MS can achieve 1-bit encoding for x-polarized waves at f_1 = 65 GHz, 2-bit encoding for two orthogonal LP waves and 3-bit encoding for CP waves at f_2 = 0.12 THz, and 1-bit encoding for two orthogonal CP waves at f_3 = 0.154 THz, realizing independent modulation channels with low crosstalk. As a proof of concept, by elaborately designing the coding sequences at different layers of MS for different frequency responses, the coding MS can integrate six independent functions, including abnormal refracted four-beam splitting, RCS reduction, abnormal reflection, double vortex beams, and spin-decoupled LCP and RCP waves. Furthermore, the integrated passive coding MS is fabricated and measured, and the measured results are in well agreement with the simulated and theoretical ones, which verifies the excellent performance of the coding MS. In addition, due to the flexibility of phase arrangement, the proposed MS can also be extended to achieve the integration of other sextuple functions. Indeed, the design scheme of the passive MS integrates space-frequency-polarization-spin multiplexing technologies, providing the capability of efficiently expanding functionality and information capacity, which can promote the development of next-generation high-capacity wireless communication systems.

References

[1] C. W. Qiu, T. Zhang, G. Hu, and Y. Kivshar, "Quo vadis, metasurfaces?" *Nano Lett.*, vol. 21, no. 13, pp. 5461–5474, Jun. 2021.

[2] F. Y. Yue *et al.*, "Vector vortex beam generation with a single plasmonic metasurface," *ACS Photonics*, vol. 3, no. 9, pp. 1558–1563, Sep. 2016.

[3] L. L. Huang *et al.*, "Three-dimensional optical holography using a plasmonic metasurface," *Nat. Commun.*, vol. 4, Nov. 2013, Art. no. 2808.

[4] X. J. Ni, Z. J. Wong, M. Mrejen, Y. Wang, and X. Zhang, "An ultrathin invisibility skin cloak for visible light," *Science*, vol. 349, no. 6254, pp. 1310–1314, Sep. 2015.

[5] C. Huang *et al.*, "Reconfigurable metasurface cloak for dynamical electromagnetic illusions," *ACS Photonics*, vol. 5, no. 5, pp. 1718–1725, May 2018.

[6] X. F. Jing, X. C. Gui, P. W. Zhou, and Z. Hong, "Physical explanation of fabry–pérot cavity for broadband bilayer metamaterials polarization converter," *J. Lightwave Technol.*, vol. 36, no. 12, pp. 2322–2327, Jun. 2018.

[7] B. Q. Lin *et al.*, "A high efficiency ultra-wideband circular-to-linear polarization conversion metasurface," *Opt. Commun.*, vol. 529, no. 15, Feb. 2023, Art. no. 129102.

[8] S. K. Ghosh, S. Das, and S. Bhattacharyya, "Terahertz wave conversion from linear to circular polarization by graphene metasurface featuring ultrawideband tunability," *J. Lightwave Technol.*, vol. 40, no. 20, pp. 6676–6684, Oct. 2022.

[9] V. Singh, S. Bhattacharyya, and R. Agrahari, "A low-profile tri-functional metasurface towards polarization conversions and absorption," *IEEE Antennas Wirel. Propag. Lett.*, pp. 1–5, May 2024.

[10] L. Nama, Nilotpal, S. Bhattacharyya, and P. K. Jain, "A metasurface-based, ultrathin, dual-band, linear-to-circular, reflective polarization converter: Easing uplinking and downlinking for wireless communication," *IEEE Antennas Propag. Mag.*, vol. 64, no. 4, pp. 100–110, Jan. 2021.

[11] M. I. Khan, Z. Khalid, and F. A. tahir, "Linear and circular-polarization conversion in x-band using anisotropic metasurface," *Sci. Rep.*, vol. 9, Mar. 2019, Art. no. 4552.

[12] H. B. Wang, Y. J. Cheng, and Z. N. Chen, "Wideband and wide-angle single-layered-substrate linear-to-circular polarization metasurface converter," *IEEE Trans. Antennas Propag.*, vol. 68, no. 2, pp. 1186–1191, Feb. 2020.

[13] A. D. Li *et al.*, "Hamiltonian hopping for efficient chiral mode switching in encircling exceptional points," *Phys. Rev. Lett.*, vol. 125, no. 18, Oct. 2020, Art. no. 187403.

[14] X. Q. Shu *et al.*, "Chiral transmission by an open evolution trajectory in a non-hermitian system," *Light-Sci. Appl.*, vol. 13, no. 1, Mar. 2024, Art. no. 65.

[15] Z. R. Huang *et al.*, "High-resolution metalens imaging polarimetry," *Nano Lett.*, vol. 23, no. 23, pp. 10 991–10 997, Nov. 2023.

[16] M. Ding *et al.*, "Broadband angular spectrum differentiation using dielectric metasurfaces," *Nat. Commun.*, vol. 15, Mar. 2024, Art. no. 2237.

[17] B. Cai, L. Wu, X. W. Zhu, Z. Z. Cheng, and Y. Z. Cheng, "Ultra-broadband and wide-angle plasmonic light absorber based on all-dielectric gallium arsenide (gaas) metasurface in visible and near-infrared region," *Results in Physics*, vol. 58, Mar. 2024, Art. no. 107509.

[18] B. Cai, X. W. Zhu, L. Wu, L. L. Yang, and Y. Z. Cheng, "Visible quintuple narrowband metasurface absorber based on gallium arsenide square cavity for multispectral sensing application," *Iee sensors journal*, vol. 24, no. 12, pp. 19 229–19 236, Jun. 2024.

[19] Y. Z. Cheng *et al.*, "Terahertz pseudo-waveform-selective metasurface absorber based on a square-patch structure loaded with linear circuit components," *Adv. Photonics Res.*, Jun. 2024, Art. no. 2300303.

[20] D. Wang *et al.*, "Transmission/reflection mode switchable ultra-broadband terahertz vanadium dioxide (vo2) metasurface filter for electromagnetic shielding application," *Surfaces and Interfaces*, vol. 49, Jun. 2024, Art. no. 104403.

[21] T. J. Cui, M. Q. Qi, X. Wan, and Q. Cheng, "Coding metamaterials, digital metamaterials and programmable metamaterials," *Light-Sci. Appl.*, vol. 3, no. 10, Oct. 2014, Art. no. e218.

[22] N. F. Yu *et al.*, "Light propagation with phase discontinuities: Generalized laws of reflection and refraction," *Science*, vol. 334, no. 6054, pp. 333–337, Oct. 2011.

[23] X. F. Jing *et al.*, "Enhancement of diffraction efficiency based on the addition principle of coded digital gratings," *J. Lightwave Technol.*, vol. 40, no. 1, pp. 136–142, Jan. 2022.

[24] J. B. Wu *et al.*, "Liquid crystal programmable metasurface for terahertz beam steering," *Appl. Phys. Lett.*, vol. 116, no. 13, Mar. 2020, Art. no. 131104.

[25] H. X. Xu *et al.*, "Dual-mode transmissive metasurface and its applications in multibeam transmitarray," *IEEE Trans. Antennas Propag.*, vol. 65, no. 4, pp. 1797–1806, Mar. 2017.

[26] W. G. Chen, C. A. Balanis, and C. R. Birtcher, “Checkerboard ebg surfaces for wideband radar cross section reduction,” *IEEE Trans. Antennas Propag.*, vol. 63, no. 6, pp. 2636–2645, Jun. 2015.

[27] J. Liu *et al.*, “Wideband rcs reduction of a slot array antenna using polarization conversion metasurfaces,” *IEEE Trans. Antennas Propag.*, vol. 64, no. 1, pp. 326–331, Jan. 2016.

[28] T. H. Liu *et al.*, “Six-mode orbital angular momentum generator enabled by helicity-assisted full-space metasurface with flexible manipulation of phase, polarization, and spatial information,” *Adv. Opt. Mater.*, vol. 10, no. 8, 2022, Art. no. 2102638.

[29] Q. Y. Wang *et al.*, “Flexible and independent control of asymmetric vortex beams based on spin multiplexing all dielectric metasurface,” *J. Lightwave Technol.*, vol. 41, no. 23, pp. 7098–7104, Dec. 2023.

[30] H. Y. Wang, J. Du, H. Wang, L. Y. Hua, and W. Pei, “Generation of spin-dependent accelerating beam with geometric metasurface,” *Adv. Opt. Mater.*, vol. 7, no. 15, 2019, Art. no. 1900552.

[31] W. Sen, W. X. Ke, and Z. Yan, “Simultaneous airy beam generation for both surface plasmon polaritons and transmitted wave based on metasurface,” *Opt. Express*, vol. 25, no. 20, pp. 23 589–23 596, Oct. 2017.

[32] X. M. Ding *et al.*, “Metasurface holographic image projection based on mathematical properties of fourier transform,” *PhotoniX*, vol. 1, no. 1, Jun. 2020, Art. no. 16.

[33] J. Kim *et al.*, “Photonic encryption platform via dual-band vectorial metaholograms in the ultraviolet and visible,” *ACS Nano*, vol. 16, no. 3, pp. 3546–3553, Mar. 2022.

[34] H. X. Xu *et al.*, “Super-reflector enabled by non-interleaved spin-momentum-multiplexed metasurface,” *Light-Sci. Appl.*, vol. 12, Mar. 2023, Art. no. 78.

[35] J. Lou *et al.*, “Calibration-free, high-precision, and robust terahertz ultrafast metasurfaces for monitoring gastric cancers,” *Proc. Natl. Acad. Sci. U. S. A.*, vol. 119, no. 43, Oct. 2022, Art. no. e2209218119.

[36] Y. Q. He *et al.*, “Tunable vo2 metasurface for reflective terahertz linear and circular polarization wavefront manipulation at two frequencies independently,” *Physica B: Condensed Matter*, vol. 681, Mar. 2024, Art. no. 415848.

[37] Q. R. Sun *et al.*, “Asymmetric transmission and wavefront manipulation toward dual-frequency meta-holograms,” *ACS Photonics*, vol. 6, no. 6, pp. 1541–1546, Jun. 2019.

[38] T. Y. Zhang *et al.*, “Frequency-multiplexed holographic-reflective coding metasurface for independent controls of surface wave and spatially propagating wave,” *Adv. Opt. Mater.*, vol. 11, no. 10, 2023, Art. no. 2202832.

[39] Y. P. Qi, H. Li, M. R. Su, and X. X. Wang, “Terahertz metasurface: Non-diffracting oam generation, multidimensional multiplexing, and sa-rcs reduction,” *J. Lightwave Technol.*, vol. 42, no. 5, pp. 1526–1537, Mar. 2024.

[40] X. Y. Luo *et al.*, “Quad-channel independent wavefront encoding with dual-band multitasking metasurface,” *Opt. Express*, vol. 29, no. 10, pp. 15 678–15 688, May 2021.

[41] S. Liu *et al.*, “Anisotropic coding metamaterials and their powerful manipulation of differently polarized terahertz waves,” *Light-Sci. Appl.*, vol. 5, May 2016, Art. no. e16076.

[42] G. W. Ding *et al.*, “Dual-helicity decoupled coding metasurface for independent spin-to-orbital angular momentum conversion,” *Phys. Rev. Appl.*, vol. 11, no. 4, Apr. 2019, Art. no. 044043.

[43] A. L. Dai *et al.*, “Multifunctional metasurfaces enabled by multifold geometric phase interference,” *Nano Lett.*, vol. 23, no. 11, pp. 5019–5026, May 2023.

[44] L. W. Wu *et al.*, “Multitask bidirectional digital coding metasurface for independent controls of multiband and full-space electromagnetic waves,” *Nanophotonics*, vol. 11, no. 12, pp. 2977–2987, May 2022.

[45] Y. B. Pan *et al.*, “Dual-band multifunctional coding metasurface with a mingled anisotropic aperture for polarized manipulation in full space,” *Photon. Res.*, vol. 10, no. 2, pp. 416–425, Feb. 2022.

[46] S. Sun *et al.*, “Spin- and space-multiplexing metasurface for independent phase controls of quadruplex polarization channels,” *Adv. Opt. Mater.*, vol. 11, no. 3, 2023, Art. no. 2202275.

[47] L. Bao, F. X. Jian, R. Y. Wu, Q. Ma, and T. J. Cui, “Full-space manipulations of electromagnetic wavefronts at two frequencies by encoding both amplitude and phase of metasurface,” *Adv. Opt. Mater.*, vol. 6, no. 4, 2021, Art. no. 2001032.

[48] H. Wang *et al.*, “Tailoring the excited and cutoff states of spoof surface plasmon polaritons for full-space quadruple functionalities,” *ACS Appl. Mater. Interfaces*, vol. 14, no. 4, pp. 6230–6238, Feb. 2022.

[49] J. Li *et al.*, “High-efficiency terahertz full-space metasurface for the transmission linear and reflection circular polarization wavefront manipulation,” *Phys. Lett. A*, vol. 428, Mar. 2022, Art. no. 127932.

[50] W. X. Yang *et al.*, “Direction-duplex janus metasurface for full-space electromagnetic wave manipulation and holography,” *ACS Appl. Mater. Interfaces*, vol. 15, no. 22, pp. 27 380–27 390, May 2023.

[51] Q. H. Fang, L. P. Wu, W. K. Pan, M. H. Li, and J. F. Dong, “Trifunctional metasurface for manipulating linearly and circularly polarized waves in transmission and reflection modes,” *Appl. Phys. Lett.*, vol. 117, no. 7, Aug. 2020, Art. no. 074102.

[52] W. X. Yang, K. Chen, J. M. Zhao, T. Jiang, and Y. J. Feng, “A wideband high-efficiency transmit-reflect-array antenna for bidirectional radiations with distinct circular polarizations based on a metasurface,” *IEEE Trans. Antennas Propag.*, vol. 71, no. 4, pp. 3695–3700, Apr. 2023.

[53] L. Zhang *et al.*, “325 ghz to 500 ghz single-layer planar goubau-line antenna with endfire radiation based on substrate mode,” *IEEE Trans. Antennas Propag.*, vol. 70, no. 9, pp. 7755–7765, Sep. 2022.

[54] Z. F. Li *et al.*, “3-d manipulation of dual-helical electromagnetic wavefronts with a noninterleaved metasurface,” *IEEE Trans. Antennas Propag.*, vol. 70, no. 1, pp. 378–388, Jan. 2022.

[55] C. X. Liu *et al.*, “Programmable manipulations of terahertz beams by transmissive digital coding metasurfaces based on liquid crystals,” *Adv. Opt. Mater.*, vol. 9, no. 22, 2021, Art. no. 2100932.

[56] Q. L. Zhang, B. J. Chen, K.-M. Shum, and C. H. Chan, “Ultra-wideband and compact terahertz planar load based on spoof surface plasmon polaritons with nickel,” *IEEE Trans. Circuits Syst. II-Express Briefs*, vol. 68, no. 6, pp. 1922–1926, Jun. 2021.

Xiaohui Tan was born in Chongqing Municipality, China. She received the B.S. degree in communication engineering from Chongqing University of Technology, China, in 2021, and the M.S. degree in communication engineering from Shanxi University, Taiyuan, China, in 2024. She is currently an RF development engineer for an iot wireless communication module company.

Rongcao Yang was born in Shanxi Province, China. She received the B.S. and M.S. degrees in electronics and information technology and the Ph.D. degree in optics from Shanxi University, Taiyuan, China, in 1995, 1997, and 2005, respectively. She was a Visiting Scholar with the Australian National University, Canberra, Australia in 2009-2010 and the University of Salford, Manchester, United Kingdom in 2014-2015, respectively.

She is currently a Professor with the School of Physics and Electronics, Shanxi University. She holds eight Chinese patents, and has authored more than 120 papers in peer-reviewed journals. Her current research interests include electromagnetic metamaterials, nanophotonic devices, and microwave and optical communications.

Shu-Lin Chen (M'20) was born in Hubei Province, China. He received the B.S. degree in electrical engineering from Fuzhou University (FZU), China, in 2012; the M.S. degree in electromagnetic field and microwave technology from Xiamen University (XMU), China, in 2015; and the Ph.D. degree in engineering from the University of Technology Sydney (UTS), Australia, in 2019. From April to July 2019, he was a Research Associate with the State Key Laboratory of Terahertz and Millimeter Waves, City University of Hong Kong (CityU). From 2019 to 2022, he was a postdoctoral researcher with the Global Big Data Technologies Centre (GBDTC), UTS, where he is currently appointed as a Lecturer.

Dr Chen's research interests include reconfigurable antennas, leaky-wave antennas, intelligent metasurfaces, and array synthesis. He received the Outstanding Master's Thesis of Fujian Province in 2015. He was a co-recipient for a number of prestigious conference paper awards, including the Honorable Mention Award in 2017 IEEE AP-S/URSI, the Best Paper Award Finalists in 2017 ISAP, the Best Paper Award in 2018 ISAPE, the First Prize of Student Paper in 2021 ACES, and the Best Young Professional Award in 2022 ISAP. He was awarded the TICRA-EurAAP Travel Grant for the 2022 EuCAP and the 2022 IEEE Antennas and Propagation Society (AP-S) Fellowship. He is serving as an Associate Editor for the IEEE Transactions on Circuits and Systems II: express briefs (TCAS-II). He also served as the Lead Guest Editor of IEEE AWPL and OJAP.

Ka Fai Chan received the B.Eng. and Ph.D. degree from the City University of Hong Kong, Hong Kong SAR, China, in 1999 and 2007, respectively.

He is currently a Senior Engineer with the State Key Laboratory of Terahertz and Millimetr Waves, City University of Hong Kong. In addition, He was the Chair of IEEE Hong Kong AP/MTT Joint Chapter in 2020 and 2021, His research interests include computational electromagnetics, millimeter-wave and terahertz application.

Bao Jie Chen (M' 18) was born in Liaoning, China, in 1984. He received the B.S. and M.S. degrees in material science from Dalian Polytechnic University, Dalian, China, in 2007 and 2010, respectively, and the Ph.D. degree in electrical engineering from the City University of Hong Kong, Hong Kong, in 2014.

He is currently an Engineer with the State Key Laboratory of Terahertz and Millimeter Waves in City University of Hong Kong. His current research interests include rare-earth-doped materials, optical amplifiers, and development of terahertz devices and components.

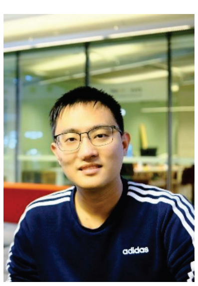

Zhao-Qi Cui was born in Shanxi Province, China. He received the B.Eng degree from School of Electrical & Electronic Engineering (Honors), University of Adelaide, Adelaide, SA, Australia in 2021.

He is currently pursuing the Ph.D. degree with the Global Big Data Technologies Centre (GBDTC), University of Technology Sydney, Ultimo, Australia. His current research interests include reconfigurable antennas, optically transparent antennas, and antenna arrays.

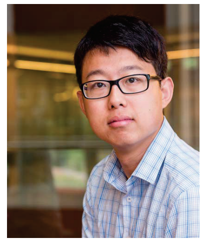

Pei-Yuan Qin was born in Liaoning Province, China, in 1983. He received a Bachelor Degree in Electronic Engineering from Xidian University, Xi'an, China, in 2006, and a joint Ph.D. Degree from Xidian University and Macquarie University, Australia, in electromagnetic fields and microwave technology in 2012. He is now an Associate Professor with University of Technology Sydney, Australia. His research interests are in the areas of reconfigurable antennas, antenna arrays, and microwave components.

Dr Qin was awarded an Australian Research Council (ARC) Discovery Early Career Researcher Award in 2017. He was awarded the Vice-Chancellor's Commendation for academic excellence by Macquarie University in 2012. He won the 2016 Computer Simulation Technology (CST) University Publication Award. He served as General Co-Chairs for 2022 IEEE International Symposium on Antennas and Propagation (ISAP) and 2019 Australian Microwave Symposium. He also served as Young Professionals Chair for AP-S/URSI 2023 and 2024. He is currently severing the Associate Editors of IEEE Transactions on Antennas and Propagation. He is the Chair of Australian Node - Antenna Measurement Techniques Association (AMTA).

Y. Jay Guo (Fellow'2014) received a Bachelor's Degree and a Master's Degree from Xidian University in 1982 and 1984, respectively, and a Ph.D Degree from Xian Jiaotong University in 1987, all in China. His current research interests include 6G antennas, mm-wave and THz communications and sensing systems as well as big data technologies. He has published six books and over 700 research papers, and he holds 27 international patents.

Jay is a Fellow of the Australian Academy of Engineering and Technology, Royal Society of New South Wales and IEEE. He has won a number of the most prestigious Australian national awards including the Engineering Excellence Awards (2007, 2012) and CSIRO Chairman's Medal (2007, 2012). He was named one of the most influential engineers in Australia in 2014 and 2015, and Australia's Research Field Leader in Electromagnetism by the Australian Research Awards for four consecutive years since 2020. Together with his students and postdocs, he has won numerous best paper awards. In 2023, Jay received the prestigious IEEE APS Sergei A. Schelkunoff Transactions Paper Prize Award. Jay is a Distinguished Professor and the Director of Global Big Data Technologies Centre (GBDTC) at the University of Technology Sydney (UTS), Australia. He is the founding Technical Director of the New South Wales (NSW) Connectivity Innovation Network (CIN) funded by NSW Telco Authority. He is also the Founding Director of the TPG-UTS Network Sensing Lab funded by TPG Telecom. Before joining UTS in 2014, Prof Guo served as a Director in CSIRO for over nine years. Prior to CSIRO, he held various senior technology leadership positions in Fujitsu, Siemens and NEC in the U.K.

Chi Hou Chan (Fellow, IEEE) received his PhD from the University of Illinois at Urbana-Champaign (UIUC), Urbana, Illinois, USA, in 1987 under the tutelage of Professor Raj Mittra. Prior to joining City University of Hong Kong in 1996, he was a tenured Associate Professor in the Department of Electrical Engineering, University of Washington, Seattle, Washington, USA. Since 1998, he has been a Chair Professor of Electronic Engineering and is currently the Director of State Key Laboratory of Terahertz and Millimeter Waves (City University of Hong Kong) and Vice President (Community Engagement). Initially trained in computational electromagnetics, his research interest has been extended to antennas, microwave and millimeter-wave components and systems, and more recently, terahertz science and technology. Professor Chan was elected a Fellow of IEEE in 2002 for his contributions to computational electromagnetics. He received the 2019 IEEE Antennas and Propagation Society Harrington-Mittra Award in Computational Electromagnetics and the 2019 Distinguished Alumni Award from the Department of Electrical and Computer Engineering, UIUC.